Pergamon

Int. J. Solids Structures Vol. 34, No. 7, pp. 799–817, 1997
© 1997 Elsevier Science Ltd
Printed in Great Britain. All rights reserved
0020–7683/97 $17.00 + .00

PII: S0020–7683(96)00055–8

AN UNSYMMETRIC DOUBLE CANTILEVER BEAM TEST FOR INTERFACIAL FRACTURE TOUGHNESS DETERMINATION

VISWANATHAN SUNDARARAMAN and BARRY D. DAVIDSON
Department of Mechanical, Aerospace and Manufacturing Engineering, Syracuse University, Syracuse, NY 13244, U.S.A.

(*Received* 16 *May* 1995; *in revised form* 16 *April* 1996)

Abstract—An unsymmetric double cantilever beam test is described and its suitability for the determination of interfacial fracture toughness is evaluated. The test specimen consists of a beam-type geometry comprised of two materials, one 'top' and one 'bottom,' with a crack at one end along the bimaterial interface. The specimen is loaded in a splitting fashion similar to that of a conventional double cantilever beam test. Due to the dissimilar in-plane and out-of-plane deformations of the two legs, the load vs deflection response of the specimen is found to be nonlinear. A nonlinear plate theory is used to predict the deformations of the specimen, and these results are used in a crack tip element analysis to determine energy release rate and mode mixity. The analytical predictions are verified by comparisons to results from two-dimensional, geometrically nonlinear finite element continuum analyses for a variety of typical materials and test geometries. It is shown that, by varying the relative thicknesses of the two materials, the unsymmetric double cantilever beam test can be used on most bimaterial pairs to determine interfacial fracture toughness over a reasonably wide range of mode mixities. © 1997 Elsevier Science Ltd. All rights reserved.

INTRODUCTION

There has been a recent resurgence of interest in the fracture of bimaterial interfaces. In part, this can be attributed to the growing use of structural surface coatings and fused and bonded connections. An additional motivation has been the need to understand failure at the fiber/matrix interface in advanced fiber composites. In-depth reviews of the efforts and advances in the bimaterial fracture problem have been presented by Shih (1991) and Hutchinson and Suo (1991). Without repeating their discussions, we point out that the majority of the advances regarding the fundamental issues of interfacial fracture, for example, the oscillatory nature of the stress singularity and the resulting ambiguity in mode decomposition, have been through theoretical studies (e.g., Williams, 1959; England, 1965; Erdogan, 1965; Rice and Sih, 1965; Rice, 1988). Progress in the *experimental* investigation of interfacial fracture has, in many respects, lagged behind, although a number of excellent test methods and specimens have recently been developed. Among others, these include symmetric and asymmetric cantilever beam sandwich specimens (Cao and Evans, 1989), the asymmetric, wedge-loaded double cantilever beam specimen (Xiao *et al.*, 1993), the notched four-point flexure specimen (Charalambides *et al.*, 1989; Cao and Evans, 1989), thin-layer sandwich specimens (Suo and Hutchinson, 1989; Thurston and Zehnder, 1993), the brazil-nut sandwich specimen (Wang and Suo, 1990), the biaxially loaded bimaterial strip (Liechti and Chai, 1991), symmetric and asymmetric three-point and four-point bend specimens (O'Dowd *et al.*, 1992), brazilian disks (O'Dowd *et al.*, 1992), and bimaterial and sandwich blister specimens (Liechti and Liang, 1992). The relatively large number of test methods and associated specimen geometries may be, in part, a response to overcome certain difficulties associated with the complexity of loading, specimen geometry and/or data reduction that are encountered in the bimaterial fracture problem. Similar concerns motivate the present work. Our primary goals were to develop a test or series of tests for which: (1) the specimens were simple to fabricate; (2) the tests could be run in a uniaxial load frame; (3) load vs deflection data from the tests could be used directly to obtain the critical energy release rate; (4) closed-form techniques could be used to extract the mode mixity from the test data; and (5) a complete range of mode mixities could be examined

for most bimaterial pairs. To this end, in this work an unsymmetric double cantilever beam (UDCB) test is described. The UDCB test, along with the recently proposed single leg bending test (Davidson and Sundararaman, 1996) and unsymmetric end-notched flexure test (Sundararaman and Davidson, 1995), appear to meet the five criteria above. Specimens for all three tests are similar and are relatively easy to fabricate. Loading fixtures and data reduction procedures for the three tests are also relatively simple, and the three tests combined can be used to determine fracture toughnesses over a complete range of mode mixities for most bimaterial pairs.

In what follows,the UDCB test for fracture of interfaces between homogeneous isotropic plates is presented and analyzed. A geometrically nonlinear plate theory is used to obtain the forces, moments and deflections in the two cracked regions of the specimen. These results are used with a closed-form crack tip element analysis (Davidson *et al.*, 1995) to predict energy release rate and mode mixity as a function of the loading and the geometric and material properties. For typical bimaterial pairs, the analytical predictions for deflections, fracture energy and mode mixity are verified by comparison to selected results from geometrically nonlinear, two-dimensional continuum finite element analyses. It is shown that the UDCB test can be used to determine the fracture toughness of any specific interface over a relatively wide range of mode mixities. Suggestions for appropriate test specimen dimensions and data reduction techniques are also presented, as is a discussion of the conditions under which linear theory may be used to obtain a reasonably good approximation for energy release rate and mode mixity.

THE UDCB TEST GEOMETRY

A schematic of the UDCB specimen and its associated loading, boundary conditions and coordinate system is shown in Fig. 1. The boundary conditions are indicative of those that would be encountered if the UDCB specimen were placed in a conventional tension load frame gripping arrangement. It is assumed that freely rotating 'loading tabs' are used (e.g., ASTM, 1994), such that only vertical loads are applied for the duration of the test. The top and bottom 'legs' (cracked regions) of the specimen may be of different thicknesses and materials, and the special case of equal thicknesses and material properties results in the conventional double cantilever beam configuration (e.g., Broek, 1986). Notice that for most other configurations, the dissimilar deflections, and hence in-plane shortening of the two legs, results in a rotation of the entire specimen and a geometrically nonlinear test.

Referring to Fig. 1, we will define material *1* to be that material with the higher Young's modulus and material *2* to be that with the lower modulus, and the subscripts *1* and *2* on various parameters will be used to denote values for materials *1* and *2*, respectively. Furthermore, material *1* will always be assigned as the 'top' leg, i.e., above the crack. Considering the loading, there is no loss in generality associated with this definition. Thus, the 'positive z' direction will always point away from material *1* and towards material *2*. The origin of the z-coordinate axis is defined to be at the geometric midplane of the uncracked region, and the origin of the x-coordinate axis is located at the crack tip. The crack itself is planar and of length a. It is initially assumed in the analysis that either

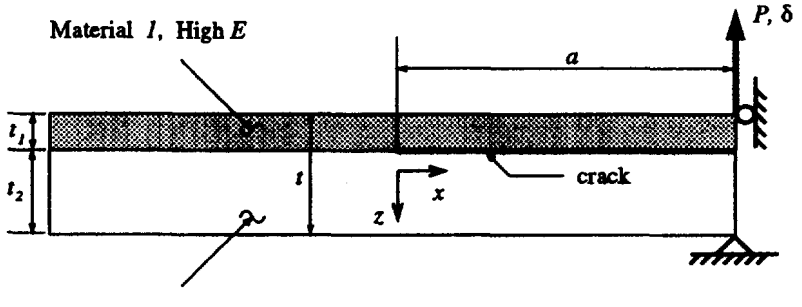

Fig. 1. Schematic of the UDCB test.

plane stress or plane strain conditions exist with respect to the y-coordinate direction. A subsequent discussion is aimed at elucidating the effects of the true constraint conditions that apply to a finite width specimen.

PLATE THEORY ANALYSIS

Analysis of deformation

Figure 2 shows the deformed shape of a UDCB specimen. It is assumed in the figure that the upper leg has a lower bending rigidity than that of the lower leg. Note that, away from the crack tip, the uncracked region remains undeformed and experiences only a rigid body rotation. Also note that the applied loading is assumed to act at the midsurface of the specimen legs, which is slightly different from the loading configuration shown in Fig. 1. This choice is made for the sake of simplicity of the closed-form nonlinear plate theory analysis of deformation. In subsequent comparisons to finite element results, the finite element model is assumed to have the boundary conditions of the physical test, as shown in Fig. 1; these results will show that the plate theory analysis, as formulated, may be used to accurately predict results for the physical test geometry. Finally, note that the definition of the crack opening displacement, δ, is chosen such that $\delta = 0$ in the absence of an applied load.

Assuming that shear deformation may be neglected, the deformations of the cracked portion of the UDCB specimen outside of the near-tip region may be obtained through a 'corrected' plate theory analysis. Similar to the classical theory, this analysis assumes that plate cross sections initially normal to the midsurface remain planar and normal to the midsurface after deformation. It is also assumed that no midplane straining of the two legs of the UDCB specimen occurs during the test, and linear constitutive equations and the small strain–displacement relations are utilized. The correction to the classical theory is one that allows for large deflections and rotations. Essentially similar approaches have been used for large displacement analyses of cantilever beams (Barten, 1944; Bisshopp and Drucker, 1945) and conventional double cantilever beam (DCB) specimens (Devitt *et al.*, 1980; Williams, 1987). To incorporate the effect of shear deformation, one could model torsional and/or extensional springs between the two materials in the uncracked region. Such approaches have been used successfully for small deflections of conventional DCB specimens (e.g., Kanninen, 1973; Weatherby, 1982; Olsson, 1992) and our results to-date show that such an approach would be necessary to accurately model a UDCB specimen

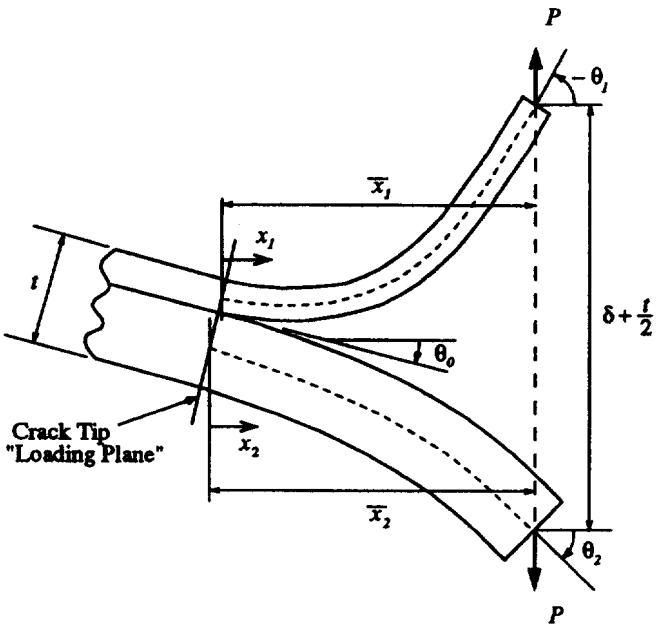

Fig. 2. Deformed configuration of the UDCB specimen.

comprised of orthotropic materials with large ratios of Young's modulus to shear modulus. However, as will be verified in a subsequent section, ignoring shear deformations produces acceptable results for those cases where materials *1* and *2* are isotropic.

With reference to Figs 1 and 2, the independent variables in the problem are the applied load, P, or the applied displacement, δ, the crack length, a, the thicknesses of the legs, t_1 and t_2, and the material properties of the regions above and below the crack plane. The primary dependent variables that need to be evaluated are θ_0, θ_1, and θ_2. All slopes are defined with respect to the x–z coordinate axes; thus, θ_0 and θ_2 as pictured are positive and the slope of the top leg at the loaded end is negative. However, in a subsequent numerical solution procedure, we prefer to search for positive θ_1 and θ_2. To this end, the end slope of the top leg will be taken to be $-\theta_1$; with this definition, θ_1 and θ_2 will always be greater than zero. The slope of the uncracked region, θ_0, may be positive, zero or negative depending on the relative bending rigidities of the two legs. Specifically, under the present choice of coordinate system, θ_0 will be positive if the flexural rigidity of the bottom leg is greater than that of the top leg. It is assumed that the test is conducted under force control (specified P); an analogous, albeit more cumbersome analysis can be performed for a UDCB specimen subjected to specified displacements.

The Euler–Bernoulli moment–curvature relationship for the midplane of either of the cracked regions of the specimen may be written as (Bisshopp and Drucker, 1945)

$$\frac{M_i(x)}{D_i} = k_i(x) = -\frac{1}{(1+s_i^2)^{3/2}}\frac{\mathrm{d}s_i}{\mathrm{d}x} \tag{1}$$

where i denotes the cracked region of interest, D_i ($i = 1, 2$) is its flexural modulus, $M_i(x)$ and $k_i(x)$ are the local bending moment and curvature at an arbitrary location x, and $s_i(x) = \tan\phi_i$, where $\phi_i(x)$ is the slope of the midsurface at any location x. For a homogeneous isotropic cracked region of modulus E_i, Poisson's ratio ν_i, and thickness t_i in plane strain ($\varepsilon_{yy} = 0$)

$$D_i = \frac{E_i' t_i^3}{12}; \quad E_i' = \frac{E_i}{(1-\nu_i^2)}. \tag{2}$$

For plane stress ($\sigma_{yy} = 0$), ν_i is set equal to zero in the above.

For subsequent use, we introduce 'local' coordinate axes, x_1 and x_2, for the top and bottom legs, respectively, as shown in Fig. 2. These local axes are utilized in the analysis of specimen deformations. For the top leg, the boundary conditions on s_1 are given by:

$$s_1(x_1 = 0) = \tan\theta_0; \quad s_1(x_1 = \bar{x}_1) = -\tan\theta_1. \tag{3}$$

Here, $\bar{x}_1$ is the moment arm from the load P to the midplane of the top leg at the crack tip cross-section as shown in Fig. 2. From equilibrium considerations

$$M_1(x_1) = P(\bar{x}_1 - x_1). \tag{4}$$

Following standard plate theory notation, the load, P, and moment, $M_1(x_1)$, are both defined on a per unit width basis.

To obtain an equation involving the primary variables θ_0 and θ_1, first substitute eqn (4) into (1) and, choosing $i = 1$, integrate from $x_1 = 0$, $s_1 = \tan\theta_0$ to an arbitrary x_1, where $s_1 = \tan\phi_1$. This yields

$$\sin\phi_1 - \sin\theta_0 = \frac{-P}{D_1}\left(x_1\bar{x}_1 - \frac{x_1^2}{2}\right). \tag{5}$$

Note from Fig. 2 that $\phi_1 = -\theta_1$ at $x_1 = \bar{x}_1$; thus

$$\bar{x}_1 = \sqrt{\frac{2D_1(\sin\theta_1 + \sin\theta_0)}{P}} \tag{6}$$

Next, solve eqn (5) for x_1 and use the expression for $\bar{x}_1$ given by eqn (6) to obtain

$$x_1 = \bar{x}_1 - \sqrt{\frac{2D_1(\sin\theta_1 + \sin\phi_1)}{P}}. \tag{7}$$

As it is assumed that no midplane straining occurs, the length of the top leg in its deformed state must equal the crack length, a. Using eqn (7), this condition may be expressed as

$$a = \int_0^{\bar{x}_1} \sqrt{1+s_1'^2}\,\mathrm{d}x_1 = -\sqrt{\frac{D_1}{2P}} \int_{\theta_0}^{-\theta_1} \frac{\mathrm{d}\phi_1}{\sqrt{\sin\theta_1 + \sin\phi_1}} \tag{8}$$

which gives one equation in the two unknowns θ_0 and θ_1.

An analysis of the deformation of the bottom leg proceeds as above, except with a sign change in the load, and results in:

$$\bar{x}_2 = \sqrt{\frac{2D_2(\sin\theta_2 - \sin\theta_0)}{P}} \tag{9}$$

$$a = \sqrt{\frac{D_2}{2P}} \int_{\theta_0}^{\theta_2} \frac{\mathrm{d}\phi_2}{\sqrt{\sin\theta_2 - \sin\phi_2}} \tag{10}$$

where D_2 is the flexural rigidity of the bottom leg. Equation (10) introduces θ_2, and is the second of three equations that need to be solved for θ_1, θ_2 and θ_0. From Fig. 2, the following relation between $\bar{x}_1$ and $\bar{x}_2$ can be deduced:

$$\bar{x}_2 = \bar{x}_1 + \frac{t}{2}\sin\theta_0 \tag{11}$$

where t is the thickness of the uncracked region (cf. Fig. 1). The third equation involving θ_0, θ_1 and θ_2 is found by substituting eqns (6) and (9) into (11) to obtain

$$\sqrt{\frac{2D_2(\sin\theta_2 - \sin\theta_0)}{P}} = \sqrt{\frac{2D_1(\sin\theta_1 + \sin\theta_0)}{P}} + \frac{t}{2}\sin\theta_0. \tag{12}$$

Equations (8), (10) and (12) are three simultaneous nonlinear equations for θ_0, θ_1 and θ_2. These may be solved for a given specimen geometry and applied load using an appropriate numerical search procedure; in this work, Newton's method is utilized. Once θ_0, θ_1 and θ_2 have been obtained, $\bar{x}_1$ and $\bar{x}_2$ may be computed from eqns (6) and (9), respectively.

For subsequent use when comparing the plate theory solutions to finite element results, the moment arm from the load P to the crack tip, $\bar{x}$, is given by

$$\bar{x} = \bar{x}_1 + \frac{t_1}{2}\sin\theta_0 = \bar{x}_2 - \frac{t_2}{2}\sin\theta_0. \tag{13}$$

Furthermore, under force controlled loading (specified P), the crack opening displacement, δ (cf. Fig. 2), can be shown to be

$$\delta = \sqrt{\frac{D_1}{2P}}\int_{-\theta_1}^{\theta_0} \frac{\sin\phi\,\mathrm{d}\phi}{\sqrt{\sin\theta_1+\sin\phi}} + \sqrt{\frac{D_2}{2P}}\int_{\theta_0}^{\theta_2} \frac{\sin\phi\,\mathrm{d}\phi}{\sqrt{\sin\theta_2-\sin\phi}} - \frac{t}{2}(1-\cos\theta_0). \tag{14}$$

Finally, note that the singularity that occurs in the integrands of eqns (8) and (10) may be avoided by rewriting the integrals, using integration by parts, as

$$\int_\alpha^\beta \frac{\mathrm{d}\phi}{\sqrt{\sin\theta\pm\sin\phi}} = \pm 2\left[\frac{\sqrt{\sin\theta\pm\sin\phi}}{\cos\phi}\right]_\alpha^\beta \mp 2\int_\alpha^\beta \frac{\sqrt{\sin\theta\pm\sin\phi}\sin\phi\,\mathrm{d}\phi}{\cos^2\phi}. \tag{15}$$

A similar approach may be used for the integrals in eqn (14).

Energy release rate determination

The total energy release rate for the UDCB specimen may be obtained by substituting the results of the previous analysis into the crack tip element equations (Schapery and Davidson, 1990; Davidson *et al.*, 1995). These equations express the total energy release rate in terms of a concentrated crack tip force, N_c, and moment, M_c. Within the context of plate theory, N_c and M_c arise to enforce displacement compatibility in the uncracked region at the interface between the upper and lower materials. A plate theory version of Irwin's (1957) virtual crack closure method yields the total energy release rate (ERR) as

$$G = \frac{1}{2}(c_1N_c^2 + c_2M_c^2 + 2\sqrt{c_1c_2}N_cM_c\sin\Gamma) \tag{16}$$

where

$$\sin\Gamma = \frac{c_{12}}{\sqrt{c_1c_2}}. \tag{17}$$

The constants c_1, c_2 and c_{12} are based on the general expressions provided by Schapery and Davidson (1990) and Davidson *et al.* (1995). For a bimaterial UDCB specimen geometry comprised of isotropic materials, they are given by:

$$c_1 = \frac{4}{E_1't_1} + \frac{4}{E_2't_2} \tag{18}$$

$$c_2 = \frac{12}{E_1't_1^3} + \frac{12}{E_2't_2^3} \tag{19}$$

$$c_{12} = \frac{6}{E_2't_2^2} - \frac{6}{E_1't_1^2}. \tag{20}$$

As before, subscripts *1* and *2* refer to the top and bottom materials, respectively. For the UDCB geometry, the quantities N_c and M_c are (Schapery and Davidson, 1990; Davidson *et al.*, 1995)

$$N_c = -N_1; \quad M_c = M_1 - \frac{N_1t_1}{2}. \tag{21}$$

Here, N_1 and M_1 are the classical plate theory in-plane force and bending moment, respectively, that are in material *1* at the crack tip. These act on the 'loading plane' depicted in Fig. 2. Considering the deformed geometry, they are given by

$$N_1 = -P\sin\theta_0; \quad M_1 = P\bar{x}_1 \tag{22}$$

where θ_0 and $\bar{x}_1$ are determined using eqns (6), (8), (10) and (12).

Mode decomposition

The crack tip element approach may also be used for the analytical determination of the stress intensity factor and mode mix. This approach will produce identical predictions as the method developed by Suo and Hutchinson (1990), and is chosen primarily to be consistent with the notation of our other works (Davidson and Sundararaman, 1996; Sundararaman and Davidson, 1995).

The complex stress intensity factor, K, can be written as (Davidson *et al.*, 1995),

$$K = \sqrt{\frac{2}{H}}\cosh\pi\varepsilon(iN_c\sqrt{c_1} + M_c\sqrt{c_2}e^{i\Gamma})T^{-i\varepsilon}e^{i\Omega_T} \tag{23}$$

where

$$H = \frac{2}{E_1'} + \frac{2}{E_2'}. \tag{24}$$

The bimaterial constant, ε, is given by

$$\varepsilon = \frac{1}{2\pi}\ln\left(\frac{1-\beta}{1+\beta}\right) \tag{25}$$

and β is a Dundurs' (1969) parameter, defined as

$$\beta = \frac{1}{H}\left[\frac{(1-\nu_2')}{E_2'} - \frac{(1-\nu_1')}{E_1'}\right] \tag{26}$$

where, for plane stress, $\nu_i' = \nu_i$, and for plane strain, $\nu_i' = \nu_i/(1-\nu_i)$.

Following Rice's (1988) suggestion, we define K_{I} and K_{II} through the equation,

$$K\hat{T}^{i\varepsilon} = K_{\mathrm{I}} + iK_{\mathrm{II}} \tag{27}$$

where $\hat{T}$ is defined to be a fixed quantity that does *not* scale with specimen size. Substituting (23) into (27) yields the individual stress intensity factors as

$$K_{\mathrm{I}} = \sqrt{\frac{2}{H}}\cosh\pi\varepsilon[-N_c\sqrt{c_1}\sin\hat{\Omega} + M_c\sqrt{c_2}\cos(\hat{\Omega}+\Gamma)] \tag{28}$$

$$K_{\mathrm{II}} = \sqrt{\frac{2}{H}}\cosh\pi\varepsilon[N_c\sqrt{c_1}\cos\hat{\Omega} + M_c\sqrt{c_2}\sin(\hat{\Omega}+\Gamma)] \tag{29}$$

where

$$\hat{\Omega} = \Omega_T + \varepsilon\ln\left(\frac{\hat{T}}{T}\right). \tag{30}$$

In eqns (23) and (30), Ω_T is the 'mode mix parameter' that determines the ratio of $K_{\mathrm{II}}/K_{\mathrm{I}}$ and T is the characteristic dimension, *which scales with specimen thickness*, upon which it is based. This characteristic dimension enters explicitly into the determination of Ω_T (Davidson *et al.*, 1995). A closed-form expression for Ω_{t_1}, i.e., Ω_T where $T = t_1$, is presented by Davidson *et al.* (1995). The relationship between Ω_T and Ω_{t_1} is given by

$$\Omega_T = \Omega_{t_1} + \varepsilon \ln\left(\frac{T}{t_1}\right). \tag{31}$$

In many cases, it may be most convenient to test UDCB specimens of a given bimaterial pair that have different thickness ratios, t_1/t_2, but the same total thickness, $t = t_1 + t_2$. If this is the case, it may be simplest to base K_{I}, K_{II} and Ω_T all on t, i.e., one could choose $T = \hat{T} = t$. This simplifies all the scaling relationships, as eqn (30) now gives $\hat{\Omega} = \Omega_t$. If the closed-form expression for the mode-mix parameter given by Davidson *et al.* (1995) is to be used, then eqn (31) gives the transformation from Ω_{t_1} to Ω_t.

The results of fracture tests of UDCB specimens with a variety of thickness ratios may be presented in the form of a $G_c(\psi_{\hat{T}})$ curve, where G_c is the critical energy release rate and $\psi_{\hat{T}}$ is equivalently referred to as the phase angle or the mode mix. It is based on the fixed distance $\hat{T}$ and is given by

$$\tan(\psi_{\hat{T}}) = \frac{K_{\mathrm{II}}}{K_{\mathrm{I}}} = \frac{N_c\sqrt{c_1}\cos\hat{\Omega} + M_c\sqrt{c_2}\sin(\hat{\Omega}+\Gamma)}{-N_c\sqrt{c_1}\sin\hat{\Omega} + M_c\sqrt{c_2}\cos(\hat{\Omega}+\Gamma)}. \tag{32}$$

This data may subsequently be used to predict fracture in geometries or test specimens of different absolute dimensions. If desired, the $G_c(\psi_{\hat{T}})$ curve may be expressed in terms of a different absolute distance, say $\hat{L}$, using the transformation,

$$\psi_{\hat{L}} = \psi_{\hat{T}} + \varepsilon \ln\left(\frac{\hat{L}}{\hat{T}}\right) \tag{33}$$

Equations (28) and (29) may also be related to the ERR components (Davidson *et al.*, 1995) to obtain

$$G_{\mathrm{I}} = \frac{1}{2}[-N_c\sqrt{c_1}\sin\hat{\Omega} + M_c\sqrt{c_2}\cos(\hat{\Omega}+\Gamma)]^2 \tag{34}$$

$$G_{\mathrm{II}} = \frac{1}{2}[N_c\sqrt{c_1}\cos\hat{\Omega} + M_c\sqrt{c_2}\sin(\hat{\Omega}+\Gamma)]^2. \tag{35}$$

The total energy release rate, $G = G_{\mathrm{I}} + G_{\mathrm{II}}$, is independent of the value of $\hat{\Omega}$ and will always equal that given by eqn (16). When $\varepsilon = 0$, the energy release rate components retain their classical definitions (in terms of σ_{zz} and τ_{xz}). When $\varepsilon \neq 0$, G_{I} and G_{II} are dimensionally convenient generalizations of the classical definitions, and their use in fracture problems is similar to the use of K_{I} and K_{II}. However, use of G_{I} and G_{II} will not indicate a possible dependence of the toughness, G_c, on the sign of $\psi_{\hat{T}}$. To allow for such possible dependence, we will subsequently express our results using G and $\psi_{\hat{T}}$.

FINITE ELEMENT VERIFICATION

In this section, the preceding analysis is verified by results from two-dimensional geometrically nonlinear finite element analyses of the UDCB specimen. Three specimen types are considered: (1) a monolithic isotropic material ($\varepsilon = 0.0$); (2) alumina/niobium (plane strain $\varepsilon = -0.0201$), with elastic properties taken from Stout *et al.* (1991); and (3) glass/epoxy (plane strain $\varepsilon = -0.0604$), with elastic properties taken from Liechti and Chai (1991). The Young's moduli and Poisson's ratios of the materials comprising the three specimen types are presented in Table 1. The choice of these specimen types essentially 'spans' the range of material property mismatch ratios that one would expect to encounter

Table 1. Material properties

Material:	Monolithic	Alumina	Niobium	Glass	Epoxy
E (GPa)	180.0	386.0	107.5	68.9	2.07
ν	0.30	0.22	0.38	0.20	0.37

in typical bimaterial applications. In all cases, mode mixity will be based on the definition given by eqn (32) with $\hat{T} = t = 3.048$ mm for all specimens. Plane strain conditions are assumed.

Finite element models

All finite element models used in this study were discretized versions of the specimen geometry shown in Fig. 1. Three different geometric models were constructed, corresponding to thickness ratios (t_1/t_2) of 1.0, 0.5 and 0.2. The total thickness, t, of each model was 3.048 mm. The total length of each model was $66.7t$ and each model included a crack with a nondimensional crack length, a/t, equal to 33.3. Thus, by appropriate placement of the loading point and boundary conditions, specimens with various crack lengths could be analyzed. In what follows, we consider four different crack lengths, corresponding to a/t values of 8.33, 16.7, 25.0 and 33.3. Also, by appropriate specification of material properties, at any crack length five different thickness ratios (t_1/t_2 equal to 5.0, 2.0, 1.0, 0.5 and 0.2) can be obtained for bimaterial specimens of both the glass/epoxy and alumina/niobium systems, and three different thickness ratios (1.0, 0.5 and 0.2) can be obtained for the homogeneous case. Geometrically nonlinear analyses were performed for all of these 52 different combinations.

All finite element analyses were performed using the commercially available finite element software ABAQUS, licensed from Hibbitt, Karlsson and Sorensen, Inc. Eight noded, isoparametric, quadrilateral plane strain continuum elements were used to construct the meshes. The loading and boundary conditions were applied in accordance with Fig. 1. The load was applied incrementally, and the equilibrium equations, with respect to the deformed geometry, were solved at each increment.

Figure 3 presents a view of the crack tip neighborhood from a typical model. This particular mesh is from the case $t_1/t_2 = 0.5$. The mesh refinement in the crack tip region is essentially the same as described by Davidson *et al.* (1995). Mesh refinement requirements as described in the above reference were generally adopted, although we did conduct our own mesh refinement studies to ascertain the independence of both Ω_t and $\psi_{\hat{T}}$ with respect to the finite element mesh. All results were obtained from models that contained square elements in the crack tip region and for which the length of the near-tip elements was 1/128

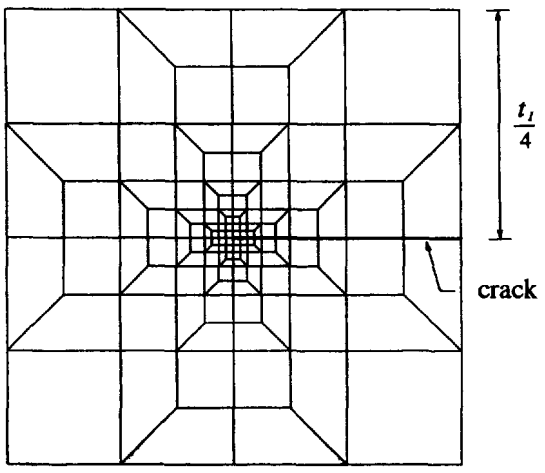

Fig. 3. Typical finite element mesh near the crack tip.

Table 2. Mode mix parameters, Ω_t (in degrees), from finite element analyses

t_1/t_2	Monolithic ($\varepsilon = 0.0$)	Alumina/Niobium ($\varepsilon = -0.0201$)	Glass/Epoxy ($\varepsilon = -0.0604$)
0.2	14.28	6.67	−14.78
0.5	7.04	−3.88	−22.31
1.0	0.00	−11.46	−25.79
2.0	−7.04	−16.82	−28.10
5.0	−14.28	−21.15	−30.99

that of the smaller of t_1 or t_2. Outside of the crack tip neighborhood, the mesh consisted solely of rectangular elements with aspect ratios between 1/10 and 10/1.

The total energy release rate, G, was always obtained by the virtual crack closure technique (Rybicki and Kanninen, 1977). Because of the large rotations that occur at the crack tip, the modified version of this technique as described by Davidson and Krafchak (1995) was adopted. Mode decomposition was accomplished using the modified crack surface displacement (CSD) method (Davidson *et al.*, 1995); this is a somewhat simpler variation of the approach originally suggested by Matos *et al.* (1989). The mode mix parameter, Ω_t, for each bimaterial pair and thickness ratio was also determined from linear runs of our finite element models using the technique described by Davidson *et al.* (1995). These values are presented in Table 2. In general, the finite element results in the table are very close to those given by the closed-form expression of Davidson *et al.* (1995). A detailed comparison between the two methods of obtaining Ω_t is presented in an earlier work (Davidson and Sundararaman, 1996).

In what follows, analytical predictions for the deformation, energy release rate and mode mixity for the various UDCB specimens are compared to the corresponding finite element results. Initially, comparisons are made between selected nonlinear plate theory results (abbreviated as NPT) and the corresponding nonlinear finite element results (abbreviated as FE). A subsequent section presents results from a linear plate theory analysis, and is accompanied by a discussion of when this simpler approach is valid. In all cases, the results from the geometrically nonlinear finite element analyses are assumed to be the most accurate. Hence, when it is stated that a value is underpredicted or overpredicted, it means that the plate theory results are smaller or larger in magnitude, respectively, than the corresponding finite element result. In an attempt to present all relevant information concisely, in many cases comparisons will be presented only for selected bimaterial pairs, thickness ratios (t_1/t_2), and/or slenderness ratios (a/t). Results for other configurations are generally described in the accompanying discussions.

Specimen deformations

Since the crack tip element equations utilize the results from the deformation analysis, an examination of the accuracy of these NPT predictions will aid significantly in understanding subsequent ERR and mode mix comparisons. Figure 4a and b presents the slope of the top leg, θ_1, as predicted by the NPT analysis vs those calculated from the FE results. The FE values were found by fitting a second order polynomial to the deformed positions of the last three nodes at the end of the appropriate cracked region (and along the midplane) and determining the slope of this line at the end point. All comparisons are in terms of a nondimensionalized load, $\bar{P}$, defined as

$$\bar{P} = Pa^2\left(\frac{1}{D_1} + \frac{1}{D_2}\right) \tag{36}$$

where P is the load per unit width. This expression was chosen simply because it separated the various curves that are presented by an amount sufficient to distinguish individual results, yet allowed us to present results for many different cases on a single graph. Also, in the interest of brevity, only the results for $a/t = 8.33$ and 33.3 are shown; at any thickness

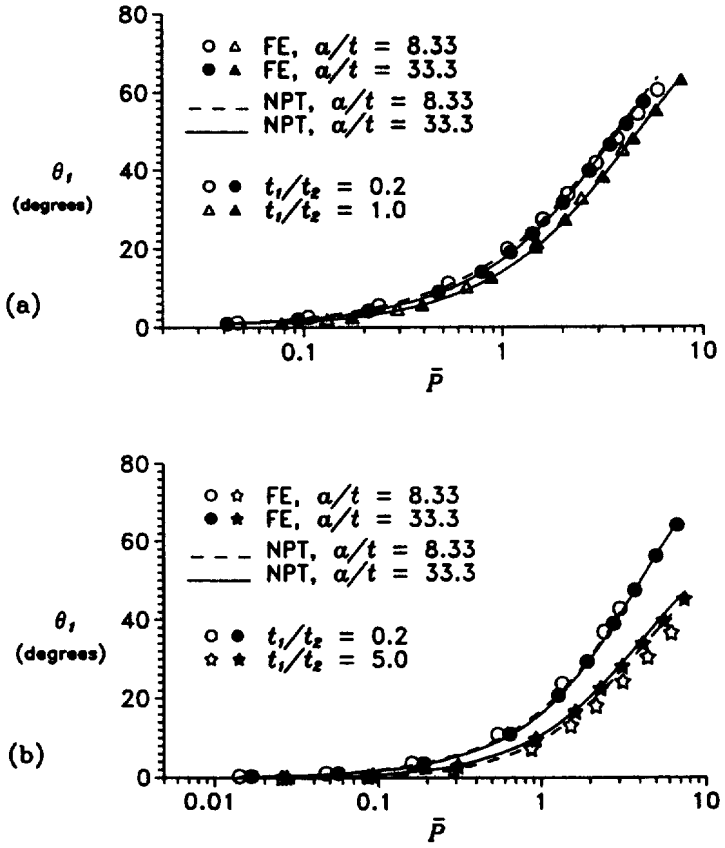

Fig. 4. Nonlinear plate theory predictions of θ_1 vs finite elements results for (a) $\varepsilon = 0.0$, (b) $\varepsilon = -0.0604$.

ratio, the percent errors in the plate theory predictions for these cases bounded those from the other two slenderness ratios. Also, only the results from the monolithic ($\varepsilon = 0.0$) and from the glass/epoxy ($\varepsilon = -0.0604$) specimens are shown, as the results from these bimaterial types bounded those for the alumina/niobium specimens. Furthermore, results only from thickness ratios of 0.2 and 1.0 for the homogeneous case, and from t_1/t_2 of 0.2 and 5.0 for the glass/epoxy bimaterial pair are presented, as these cases bounded the results from the other thickness ratios for each bimaterial system in Fig. 4a and b. All plate theory results are represented by continuous curves; dashed curves represent $a/t = 8.33$ and solid curves depict $a/t = 33.3$. All FE results are depicted using discrete symbols.

The results of the figures indicate that, in general, the nonlinear plate theory predictions for the end slope of the top leg are quite good and tend to increase in accuracy with increasing slenderness ratio. Similar trends were also observed for the end slope of the bottom leg, θ_2, and for the slope of the crack tip cross-section, θ_0. The worst correlation is for θ_2 at $t_1/t_2 = 0.2$ for the monolithic case, and for θ_1 at $t_1/t_2 = 5.0$ for the glass/epoxy. In both cases, the NPT overpredicts the corresponding FE values, and in both cases this 'worse case' correlation is for the end slope of the leg that has the highest bending rigidity of all possible combinations investigated for that particular bimaterial pair. The difference in θ_0 between the FE and NPT predictions essentially follows the larger of θ_1 or θ_2; larger errors in the end slope correspond to larger errors in the slope of the uncracked region. Overall, in all cases the correlation is quite good. Also, as would be expected, the value of θ_0 is very close to the end slope of the leg with the higher bending rigidity when the mismatch in bending rigidities of the legs is large.

Perhaps more illuminating are the results for the total opening deflection, δ, and the moment arm, $\bar{x}$. Comparisons between the FE and NPT predictions for the monolithic case are presented in Figs 5 and 6. The definition of δ^{FE} is analogous to that used for the crack opening displacement in the plate theory analysis, i.e., it is chosen such that $\delta^{FE} = 0$ when

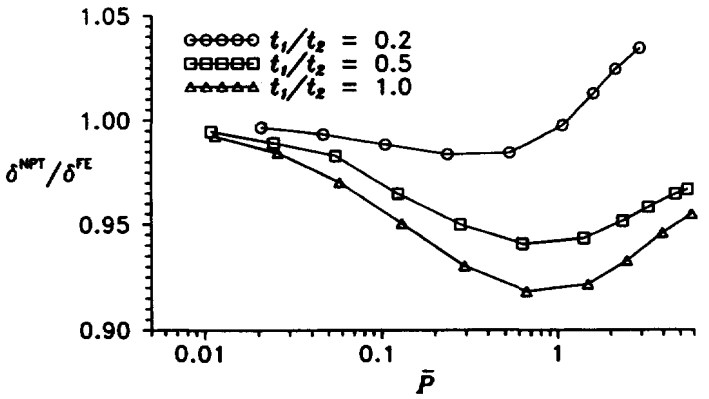

Fig. 5. Nonlinear plate theory predictions of opening deflection versus finite element results for $\varepsilon = 0.0$ and $a/t = 8.33$.

$P = 0$. These results are at a/t equal to 8.33, and the correlation between the NPT and FE results improves with increasing slenderness ratio. The response of the specimens with thickness ratios of $t_1/t_2 = 0.2$ and $t_1/t_2 = 1.0$ are markedly different, and will therefore be discussed separately; the third thickness ratio, $t_1/t_2 = 0.5$, is observed to display elements of both.

For the case where the leg thicknesses are equal, the NPT predictions for deflection, δ, are smaller than the corresponding FE results for all $\bar{P}$. This underprediction of δ with $\bar{P}$ is expected in view of the fact that the NPT neglects shear deformations. The initial decrease in δ^{NPT}/δ^{FE} with $\bar{P}$ is primarily caused by shear deformations near the crack tip. These shear deformations result in greater apparent root (near-tip) rotations of the cracked regions of the FE model as compared to the NPT results. As $\bar{P}$ becomes large, the gradual relative increase of the NPT deflections as compared to the FE predictions is a result of the increasing value of the membrane stress that occurs in the FE model; this effect is also ignored in the NPT analysis. That is, the relative stiffness of the FE model increases as more load is carried through membrane forces. With reference to $\bar{x}$ in Fig. 6, for $t_1/t_2 = 1.0$, $\bar{x}$ is overpredicted for all $\bar{P}$. Note that the predictions of $\bar{x}$ do *not* improve after the ratio of deflections (Fig. 5) begins to increase. Rather, the increased root rotation of the FE model causes a more rapid decrease of $\bar{x}$ in the FE than the NPT results, despite the stiffening of the FE model that occurs due to membrane effects. All of these and subsequent observations were verified by overlaying the deformed shapes as predicted by the FE and NPT models, as well as by examining the FE predictions for the midplane straining of the cracked regions. One other interesting observation is the relatively good correlations of θ_1 (cf. Fig. 4a) and θ_2. That is, the FE deflections are larger, but both methods predict essentially the same slope for the outer portion of the cracked regions.

Now, consider the case where $t_1/t_2 = 0.2$. Under small loads, the comparison is similar to that described above: shear deformations cause an effective larger root rotation in the

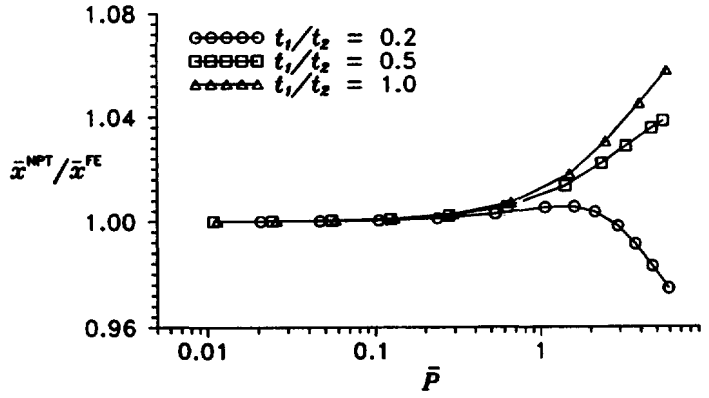

Fig. 6. Nonlinear plate theory predictions of $\bar{x}$ vs finite element results for $\varepsilon = 0.0$ and $a/t = 8.33$.

FE model. Thus, the NPT predictions for δ are smaller, and its predictions for $\bar{x}$ are larger. As the deflection increases, the FE model predicts that an appreciable amount of membrane straining occurs in the thinner region. This is because the thin region accounts for the majority of the deflection in this specimen (cf. Fig. 2). As in the symmetric case, this stiffens the FE model's response. However, in this asymmetric case, the membrane stresses also cause the rotation of the uncracked region, θ_0, to be smaller than would otherwise be predicted. Thus, the NPT begins to overpredict θ_0, θ_1 and θ_2 (cf. Fig. 4a) and the trends in δ^{NPT}/δ^{FE} and $\bar{x}^{NPT}/\bar{x}^{FE}$ reverse: the NPT begins to overpredict deflection and underpredict $\bar{x}$. With reference to Fig. 6, the $t_1/t_2 = 0.5$ specimen shows trends similar to the $t_1/t_2 = 1.0$ case at low $\bar{P}$, and begins to display elements of the $t_1/t_2 = 0.2$ case as $\bar{P}$ increases. These behaviors are also evidenced by all of the bimaterial specimens, and the above discussions, along with a consideration of the relative bending rigidities of the two regions, may be used to understand the observed results.

Energy release rate

Figures 7 and 8 present comparisons between NPT and finite element ERR predictions as a function of thickness ratio, slenderness ratio and nondimensional load. As for previous comparisons, the errors in the NPT predictions for the monolithic and glass/epoxy specimens bound those for the alumina/niobium, and results for this latter specimen are therefore not presented. Figure 7a and b presents results for the monolithic case ($\varepsilon = 0.0$) for slenderness ratios of 8.33 and 33.3, respectively. For all three thickness ratios, the NPT underpredicts G at small loads; this is primarily due to the neglect of shear deformations in the NPT analysis. For $t_1/t_2 = 1.0$ and 0.5, the overprediction of $\bar{x}$, Fig. 6, causes the NPT predictions to improve with increasing $\bar{P}$. That is, overprediction of these quantities tends to compensate for the neglect of shear deformation [cf. eqns (13), (16), (21) and (22)]. The

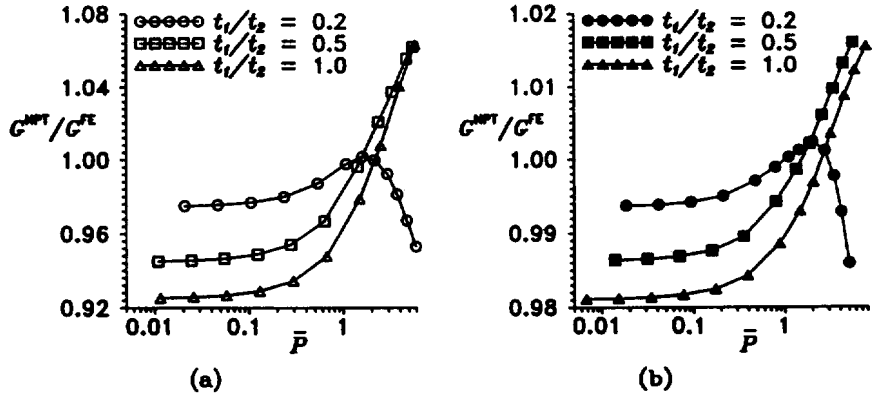

Fig. 7. Comparison of energy release rates from nonlinear plate theory and finite element analyses for $\varepsilon = 0.0$ and (a) $a/t = 8.33$, (b) $a/t = 33.3$.

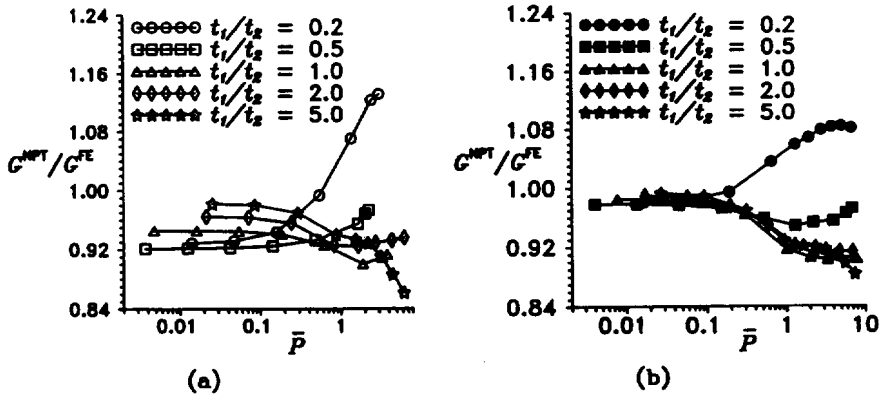

Fig. 8. Comparison of energy release rates from nonlinear plate theory and finite element analyses for $\varepsilon = -0.0604$ and (a) $a/t = 8.33$, (b) $a/t = 33.3$.

differences in the NPT and FE results for the $t_1/t_2 = 0.2$ specimen are also due to the effects of shear deformation and the differences in the predicted value of $\bar{x}$. In this case, however, $\bar{x}$ is *underpredicted* (cf. Fig. 6), which causes the observed reversal in the curve. Additionally, the plate theory analysis does not account for the effect of the membrane stresses on G. Overall, the predicted values of G for the monolithic case are quite good, and a comparison of the vertical scales in Fig. 7a and b shows that the NPT predictions improve with increasing slenderness ratio.

Results for the glass/epoxy specimens are shown in Fig. 8a and b. At thickness ratios of 0.2 and 0.5, the ratios of bending rigidities are similar to the 0.5 and 1.0 monolithic geometries. The trends in accuracy of the NPT ERR predictions are also similar, except the effect of shear deformation on ERR is more pronounced for the bimaterial specimens. At thickness ratios of 1.0, 2.0 and 5.0, the ratios of bending rigidities in the various glass/epoxy specimens are close to or larger than that for the $t_1/t_2 = 0.2$ monolithic case. However, the effect of shear deformation on ERR for the three largest thickness ratios of the bimaterial samples is more pronounced than the $t_1/t_2 = 0.2$ monolithic case. In the bimaterial samples, the ratios of ERR never rise above 1.0 for these three geometries. The glass/epoxy specimen with a thickness ratio of 5.0 shows the worst correlation due to the early and significant onset of membrane straining. As in all previous comparisons, the NPT predictions are seen to improve with increasing a/t.

Mode mixity

Figure 9 shows the range of phase angles that occur for the various geometries and bimaterial pairs. Due to the nonlinearity, the phase angle, ψ_f, for any particular geometry depends on the load. To limit the presentation, the results of Fig. 9 are presented at the critical load where fracture is expected to occur for a specimen with slenderness ratio of 8.33. The notation used in the figure, $(\psi_f)_c$, refers to the value of ψ_f that is predicted by the nonlinear plate theory analysis when the load reaches its critical value, i.e., $P = P_c$ when $G^{NPT} = G_c$. Fracture toughnesses as a function of mode mixity for the glass/epoxy specimens that are considered in this work were taken from the results presented by Liechti and Chai (1992). Note that, in their 1992 paper, Liechti and Chai reported slightly different values of elastic properties ($\varepsilon = -0.0605$) from those presented in their 1991 work ($\varepsilon = -0.0604$); however, it was assumed that this slight change in ε would not affect the interfacial toughness of the glass/epoxy system. Toughnesses for the alumina/niobium specimens were determined from the work of Stout *et al.* (1991). Selected toughness vs mode mix results for these two interfaces are presented in Table 3. For the monolithic case, G_c was taken to be 1750 J/m^2, independent of mode mixity. In general, the change in ψ_f with load is small in the plate theory analyses: for all three specimen types and all geometries of the present study, the variation in ψ_f is less than 0.9° over the range of loads considered, and ψ_f is observed to decrease monotonically with increasing load. It is interesting to note that the range of mode mixities that can be induced in the UDCB test becomes smaller as the magnitude of the

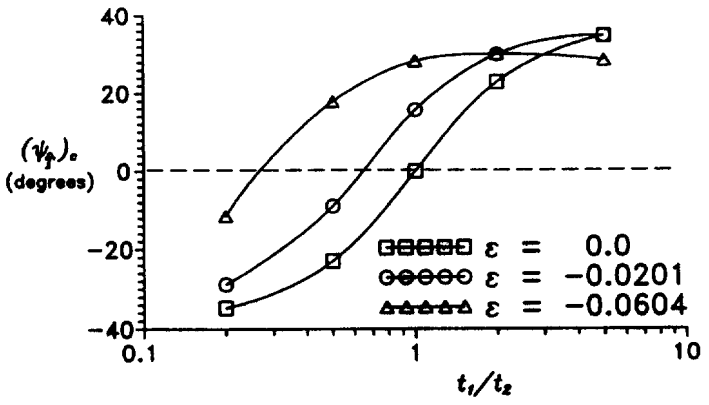

Fig. 9. Mode mixity vs thickness ratio as predicted by the nonlinear plate theory analysis for different bimaterial pairs.

Table 3. Toughness (in J/m^2) vs mode mix for Alumina/Niobium and Glass/Epoxy

	Alumina/Niobium		Glass/Epoxy	
t_1/t_2	$(\psi_f)_c$	G_c	$(\psi_f)_c$	G_c
0.2	−28.80°	64	−11.44°	4.0
0.5	−8.88°	106	17.86°	6.5
1.0	15.68°	334	28.28°	12.0
2.0	29.98°	575	30.07°	12.5
5.0	34.78°	631	28.49°	12.0

bimaterial constant, ε, increases. This is in contrast to results from the recently proposed single leg bending (SLB) test (Davidson and Sundararaman, 1996), where the range of mode mixities increases with increasing ε. The SLB test induces ranges of phase angles outside the range caused by the UDCB test; for example, for the glass/epoxy specimens, the range of mode mixities induced by the SLB test is $-56° \leqslant \psi_f \leqslant -34°$ and $29° \leqslant \psi_f \leqslant 49°$. Fracture toughness testing at large magnitude phase angles may be performed using the recently proposed unsymmetric end-notched flexure (UENF) test (Sundararaman and Davidson, 1995).

Comparisons between the analytical predictions and finite element results for mode mixity are presented in Fig. 10a and b. This figure presents the difference in ψ_f as predicted by the NPT and FE methods at critical load ($P = P_c$). This difference, $(\Delta\psi_f)_c$, is defined as

$$(\Delta\psi_f)_c = (\psi_f)_c^{\mathrm{NPT}} - (\psi_f)_c^{\mathrm{FE}} \tag{37}$$

The accuracy of the NPT predictions for the alumina/niobium sample falls between the results shown for the monolithic and glass/epoxy cases. In general, the accuracy of the NPT analysis for mode mix is very good at all slenderness ratios, with a gradual improvement with increasing a/t. If one accepts the FE results as being highly accurate, then the shape of the G_c vs ψ_f curve will determine whether a 1–2° 'error' in ψ_f is important (i.e., whether the NPT predictions may be used, without the need for FE analyses); in most cases this error will be negligible compared to the scatter in the experimental data. In terms of assessing absolute accuracy, based on the results presented in Davidson *et al.* (1995), as well as those of the original verification study of the crack surface displacement method of obtaining phase angles (Matos *et al.*, 1989), the accuracy of the FE based CSD method is very good. However, it is uncertain whether it is better than approximately 1°. Thus, it could be argued that either the FE or NPT values may be used with virtually the same accuracy. Finally, we point out that we have chosen to represent the error in ψ_f in degrees, rather than percent, because we believe this is a more meaningful measure. For example, if the error in ψ_f were measured in percent, then it is implicit that under a loading which produces a phase angle of 1°, a 2° error in phase angle is more important than for a loading

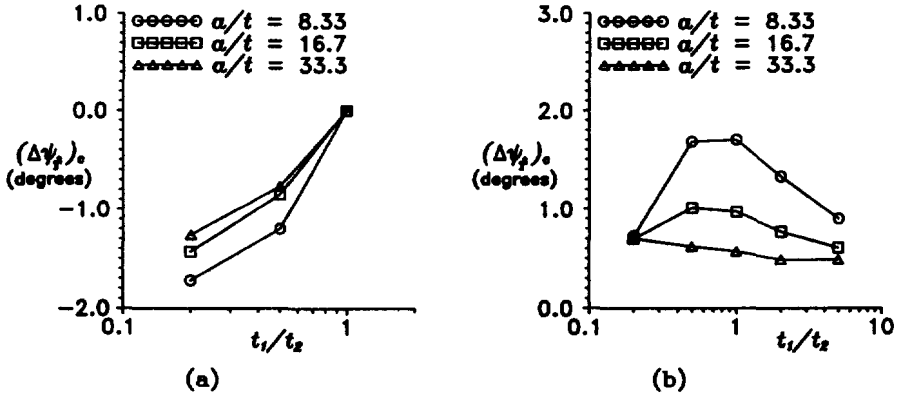

Fig. 10. Comparison of phase angles from nonlinear plate theory analysis and finite element results for (a) $\varepsilon = 0.0$, (b) $\varepsilon = -0.0604$.

which produces a phase angle of 90°. We do not believe this to be the case. The convention of showing the error in phase angle in degrees is also adopted in our works describing the SLB and UENF tests (Davidson and Sundararaman, 1996; Sundararaman and Davidson, 1995).

TEST DESIGN AND DATA REDUCTION

For a given bimaterial pair of interest, there are a number of considerations in 'designing' the UDCB test, i.e., in determining plate thicknesses, crack lengths, specimen lengths and specimen widths to obtain fracture toughness data at the mode mix of interest. These considerations are discussed below and are used to make test design and data reduction recommendations.

Finite width effects

As described in more detail in a previous work (Davidson and Sundararaman, 1996), there are two types of constraint conditions that must be considered in tests of beam-type specimens: global and local. The global conditions are scaled by the aspect (length-to-width) ratio of the specimen and are reflected in the effective bending rigidities of the two cracked regions, the opening displacement, and the total ERR. Very small aspect ratio plates will globally be in plane strain (with respect to the width direction), and very large aspect ratio plates will globally be in plane stress. The local conditions, for the small scale yielding conditions assumed herein, depend on the proximity to a free edge (normal vector parallel to y) of a particular point near the crack front. That is, consider a problem where the plate width, b, is large. In the interior of the plate, the characteristic distance that scales the K-field is given by R_k, where R_k is the smaller of t_1 or t_2. Points near the crack front that are several times R_k away from the free edge will locally be in plane strain. Using the results of Nakamura (1991; 1992) and Nakamura and Parks (1988; 1989) as a guide, it is likely that locally plane strain conditions apply, for the in-plane field, for near-crack front points that are greater than approximately $0.03R_k$ from a free surface; closer than this to the edge, the corner singularity field begins to dominate. The local conditions are reflected in the mode mix; the above indicates that for typical geometries, locally plane strain conditions predominate for the in-plane field for the majority of the specimen's width.

Based on the above, it is certainly most desirable to design a test for which both the local and global constraint conditions are plane strain. Otherwise, possible non-uniformities in the ERR and mode mix along the crack front and possible non-self-similar crack advance significantly complicate data reduction, and make it difficult or impossible to experimentally obtain a meaningful measure of fracture toughness at a given mode mix (Davidson and Schapery, 1988; Davidson, 1990). Plane strain conditions are preferable, as the ERR and mode mix will be constant along the crack front. For a finite width specimen, this will be true everywhere but in the regions near the free edges, where the corner singularity fields become important. If these regions are small with respect to the width, then the crack front will remain essentially straight during advance, the effects of the near-edge regions on test results may be considered negligible, and data reduction and interpretation are relatively straightforward. Using the results herein along with those for laminated composites (Davidson and Schapery, 1988; Davidson, 1990; Davidson *et al.*, 1996), we would recommend using test geometries for isotropic, bimaterial UDCB specimens with aspect ratios (a/b) approximately equal to 1.0, and slenderness ratios (a/t) as large as possible. Small aspect ratio plates are preferable, as this reduces the amount of transverse curvature and the associated variation in ERR across the specimen's width. Large slenderness ratios, and hence large width-to-thickness ratios as well, increase the accuracy of the plate theory analysis while simultaneously reducing the influence of any nonuniformities in ERR or mode mix at the free edges. We have found that the limitation on slenderness ratio generally comes in the form of applied load; large slenderness ratio plates may have fracture loads that are below the sensitivity of a given load cell.

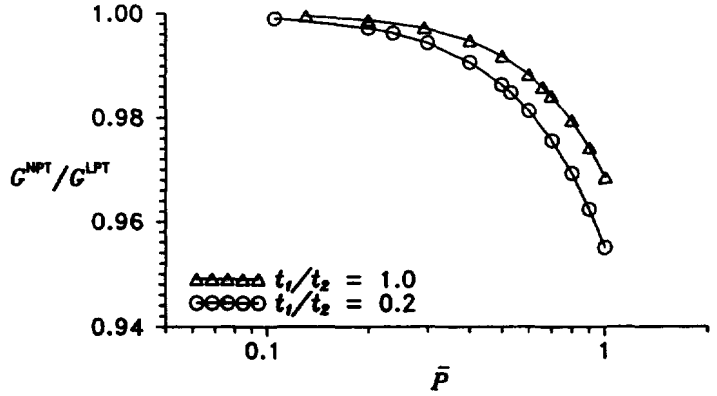

Fig. 11. Comparison of energy release rates from linear and nonlinear plate theory analyses for $\varepsilon = 0.0$ and $a/t = 8.33$.

On the use of linear theory

Figure 11 shows a comparison of ERR from linear and nonlinear plate theory analyses, denoted as 'LPT' and 'NPT,' respectively. These two curves are for a homogeneous UDCB specimen ($\varepsilon = 0.0$) at a slenderness ratio of 8.33. These two curves have been found to bound the results for all bimaterial pairs, slenderness ratios and thickness ratios studied to-date. The LPT results are found from eqns (16)–(21); in lieu of eqn (22), the linear relations

$$N_1 = 0; \quad M_1 = Pa \tag{38}$$

are used. Equivalently, these results can be reduced to give

$$G^{\mathrm{LPT}} = \frac{(\bar{P})^2}{2a^2}\left(\frac{D_1 D_2}{D_1 + D_2}\right). \tag{39}$$

The predictions for mode mixity by the linear plate theory analysis are compared to corresponding results from nonlinear finite element runs for $a/t = 8.33$ in Fig. 12. The LPT results are obtained from eqns (21), (28), (29), (32) and (38). For larger slenderness ratios, the agreement in mode mixity improves from that which is shown. Also, for each of the three bimaterial cases considered, curves are shown only for the 'extreme thickness ratios' ($t_1/t_2 = 0.2$ and 1.0 for the homogeneous case, and $t_1/t_2 = 0.2$ and 5.0 for the alumina/

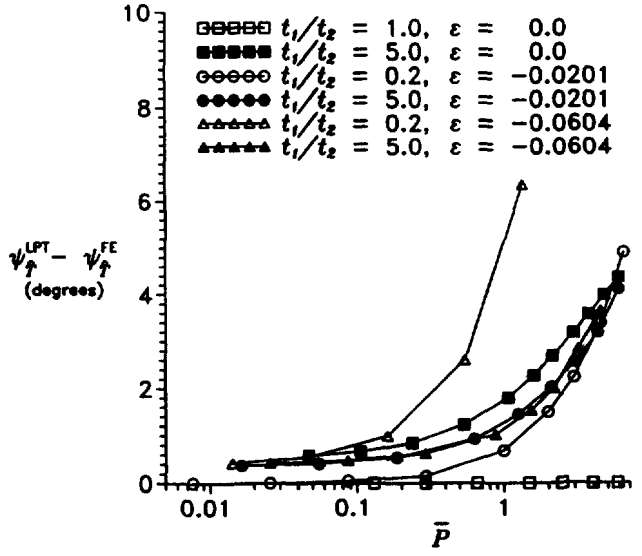

Fig. 12. Comparison of phase angles from linear plate theory analysis and finite element results for different bimaterial pairs. For $a/t = 8.33$.

niobium and glass/epoxy systems), which bound all of the results from the remaining thickness ratios.

Figures 4, 11 and 12 indicate that the accuracy of LPT is quite good for $\bar{P} \leqslant 1.0$. For the homogeneous and alumina/niobium cases, the maximum discrepancy in phase angle for the geometries studied, for $\bar{P} \leqslant 1.0$, is approximately 2°. For the glass/epoxy case, the discrepancy in phase angles between LPT and FE is approximately 6° for $t_1/t_2 = 0.2$ and $\bar{P} = 1.0$. However, for this particular glass/epoxy UDCB specimen, the critical load, $\bar{P}_c$, was predicted to equal 0.093 (using either the NPT or the nonlinear finite element analysis, and the toughness values of Table 3). For this case, at $\bar{P} = \bar{P}_c$, the discrepancy in ψ_T between the LPT and FE results is less than 1°. These results indicate that, if an estimate of G_c at the mode mix of interest (corresponding to a chosen t_1/t_2 between 0.2 and 5.0) is known *a priori*, then a specimen geometry can often be chosen such that $\bar{P}_c$ is less than 1.0 (i.e., where $G^{\text{LPT}} = G_c$). In such a case, interpolation of the curves of Fig. 12 may indicate that a nonlinear analysis is unnecessary.

Data reduction

Regardless of the analysis that is used (LPT, NPT or FE), it is our recommendation that an area method of data reduction (e.g., Whitney *et al.*, 1984) be used. This approach removes any uncertainty in geometrical or material properties from the observed toughness. Note that if the mode mix parameter, Ω_t, is obtained from the expression given by Davidson *et al.* (1995), this approach obviates the need for any finite element analyses. The choice of whether ψ_T is obtained by LPT or NPT may be made based on the observed values of $\bar{P}_c$, as well as the (non)linearity of the experimental load vs deflection data.

CONCLUSIONS

An unsymmetric double cantilever beam test has been described and evaluated for its suitability for the determination of interfacial fracture toughness. An analytical solution to obtain ERR and mode mix in typical UDCB geometries has been presented and compared to finite element predictions. These results have shown that the UDCB test may be used to determine the fracture toughness of most bimaterial interfaces over a reasonably large range of mode mixities.

The decision on whether or not to perform a FE analysis of the UDCB geometry is, of course, up to the user. Based on the results in a previous work (Davidson and Sundararaman, 1996), values of Ω_t for use in the crack tip element equations can be obtained from the expression given by Davidson *et al.* (1995) to an accuracy of approximately 2°. Essentially this same accuracy in ψ_T is obtained using this value of Ω_t and the plate theory equations. If the experimental results, in terms of the dependence of and scatter in the G_c vs ψ_T curve indicate that this accuracy is sufficient, then it is likely that FE analyses are not required. The combination of the UDCB, the single leg bending (Davidson and Sundararaman, 1996), and the unsymmetric end-notched flexure tests (Sundararaman and Davidson, 1995) provide a means by which a relatively simple test specimen geometry can be used to determine the fracture toughness of most bimaterial interfaces over a complete range of mode mixities.

Acknowledgements—This work was supported by the National Science Foundation under Grant MSS-9210844.

REFERENCES

ASTM Standard D5228-94. (1994) Standard test method for mode *I* interlaminar fracture toughness of unidirectional reinforced polymer matrix composites. *DCB Standard*, American Society for Testing and Materials.

Barten, H. J. (1944) On the deflection of a cantilever beam. *Quarterly Applied Mathematics* **2**, 168–171.

Bisshopp, K. E. and Drucker, D. C. (1945) Large deflection of cantilever beams. *Quarterly Applied Mathematics* **3**, 272–276.

Broek, D. (1986) *Elementary Engineering Fracture Mechanics*, 4th Edn. Kluwer Academic, Dordrecht.

Cao, H. C. and Evans, A. G. (1989) An experimental study of the fracture resistance of bimaterial interfaces. *Mechanics of Materials* **7**, 295–304.

Charalambides, P. G., Lund, J., Evans, A. G. and McMeeking, R. M. (1989) A test specimen for determining the fracture resistance of bimaterial interfaces. *Journal of Applied Mechanics* **56**, 77–82.

Davidson, B. D. (1990) An analytical investigation of delamination front curvature in double cantilever specimens. *Journal of Composite Materials* **24**, 1124–1137.

Davidson, B. D., Hu, H. and Schapery, R. A. (1995) An analytical crack tip element for layered elastic structures. *Journal of Applied Mechanics* **62,** 294–305.
Davidson, B. D. and Krafchak, T. M. (1995) A comparison of energy release rates for locally buckled laminates containing symmetrically and asymmetrically located delaminations. *Journal of Composite Materials* **29,** 700–713.
Davidson, B. D., Krüger, R. and König, M. (1996) Effect of stacking sequence on energy release rate distributions in multidirectional DCB and ENF specimens. Submitted to *Engineering Fracture Mechanics*.
Davidson, B. D. and Schapery, R. A. (1988) Effect of finite width on deflection and energy release rate of an orthotropic double cantilever specimen. *Journal of Composite Materials* **22,** 640–656.
Davidson, B. D. and Sundararaman, V. (1996) A single leg bending test for interfacial fracture toughness determination. Submitted to *International Journal of Fracture*.
Devitt, D. F., Schapery, R. A. and Bradley, W. L. (1980) A method for determining the mode I delamination fracture toughness of elastic and viscoelastic composite materials. *Journal of Composite Materials* **14,** 270–285.
Dundurs, J. (1969) *Journal of Applied Mechanics* **36,** 650–652.
England, A. H. (1965) A crack between dissimilar media. *Journal of Applied Mechanics* **32,** 400–402.
Erdogan, F. (1965) Stress distribution in bonded dissimilar materials with cracks. *Journal of Applied Mechanics* **32,** 403–410.
Hutchinson, J. W. and Suo, Z. (1991) Mixed mode cracking in layered materials. *Advances in Applied Mechanics* **29,** 63–191.
Irwin, G. R. (1957) Analysis of stresses and strains near the end of a crack traversing a plate. *Journal of Applied Mechanics* **24,** 361–364.
Kanninen, M. F. (1973) An augmented double cantilever beam model for studying crack propagation and arrest. *International Journal of Fracture* **9,** 83–92.
Liechti, K. M. and Chai, Y. S. (1991) Biaxial loading experiments for determining interfacial fracture toughness. *Journal of Applied Mechanics* **58,** 680–687.
Liechti, K. M. and Chai, Y. S. (1992) Asymmetric shielding in interfacial fracture under in-plane shear. *Journal of Applied Mechanics* **59,** 295–304.
Liechti, K. M. and Liang, Y. M. (1992) The interfacial fracture characteristics of bimaterial and sandwich blister specimens. *International Journal of Fracture* **55,** 95–114.
Matos, P. P. L., McMeeking, R. M., Charalambides, P. G. and Drory, M. D. (1989) A method for calculating stress intensities in bimaterial fracture. *International Journal of Fracture* **40,** 235–254.
Nakamura, T. (1991) Three-dimensional stress fields of elastic interface cracks. *Journal of Applied Mechanics* **58,** 939–946.
Nakamura, T. (1992) Three dimensional interface cracks of elastic plates. In *Fracture Mechanics: Twenty Second Symposium*, (Edited by H. A. Ernst, A. Saxena and D. L. McDowell) ASTM STP **1131,** pp. 635–649.
Nakamura, T. and Parks, D. M. (1988) Symmetrical stress field near the crack front of a thin elastic plate. *Journal of Applied Mechanics* **55,** 805–813.
Nakamura, T. and Parks, D. M. (1989) Antisymmetrical 3-D stress fields near the crack front of a thin elastic plate. *International Journal of Solids and Structures* **25,** 1411–1426.
O'Dowd, N. P., Shih, C. F. and Stout, M. G. (1992) Test geometries for measuring interfacial fracture toughness. *International Journal of Solids and Structures* **29,** 571–589.
Olsson, R. (1992) A simplified improved beam analysis of the DCB specimen. *Composites Science and Technology* **43,** 329–338.
Rice, J. R. (1988) Elastic fracture mechanics concepts for interfacial cracks. *Journal of Applied Mechanics* **55,** 98–103.
Rice, J. R. and Sih, G. C. (1965) Plane problems of cracks in dissimilar media. *Journal of Applied Mechanics* **32,** 418–423.
Rybicki, E. F. and Kanninen, M. F. (1977) A finite element calculation of stress intensity factors by a modified crack closure integral. *Engineering Fracture Mechanics* **9,** 931–938.
Schapery, R. A. and Davidson, B. D. (1990) Prediction of energy release rates for mixed-mode delamination using classical plate theory. *Applied Mechanics Review* **43,** S281–S287.
Shih, C. F. (1991) Cracks on bimaterial interfaces: elasticity and plasticity aspects. *Materials Science Engineering* **A143,** 77–90.
Stout, M. G., O'Dowd, N. P. and Shih, C. F. (1991) Interfacial fracture toughness of alumina/niobium systems. In *Experiments in micromechancis of failure resistant materials* presented at ASME Winter Annual Meeting, Atlanta, Georgia, 1–6 December, (Edited by K.-S. Kim) ASME AMD **130,** pp. 9–16.
Sundararaman, V. and Davidson, B. D. (1995) An unsymmetric end notched flexure test for interfacial fracture toughness determination. Syracuse University Department of Mechanical, Aerospace and Manufacturing Engineering technical report number 94–202.
Suo, Z. and Hutchinson, J. W. (1989) On sandwich test specimens for measuring interface crack toughness. *Materials Science Engineering* **A107,** 135–143.
Suo, Z. and Hutchinson, J. W. (1990) Interface crack between two elastic layers. *International Journal of Fracture* **43,** 1–18.
Thurston, M. E. and Zehnder, A. T. (1993) Experimental determination of silica/copper interfacial toughness. *Acta Metallica Materiala* **41,** 2985–2992.
Wang, J. S. and Suo, Z. (1990) Experimental determination of interfacial toughness curves using Brazil-nut-sandwiches. *Acta Metallica Materiala* **38,** 1279–1290.
Weatherby, J. R. (1982) Evaluation of energy release rates in unidirectional double cantilevered beam fracture specimens. *Mechanics and Materials Report Number MM*4665-82-9, Master's thesis, Texas A&M University.
Whitney, J. M., Daniel, I. M. and Pipes, R. B. (1984) *Experimental mechanics of fiber reinforced composite materials*. Society for Experimental Mechanics Monograph Number 4.
Williams, J. G. (1987) Large displacement and end block effects in the DCB interlaminar test in modes I and II. *Journal of Composite Materials* **21,** 330–348.
Williams, M. L. (1959) The stresses around a fault or crack in dissimilar media. *Bulletin of the Seismic Society of America* **49,** 199–204.
Xiao, F., Hui, C. Y. and Kramer, E. J. (1993) Analysis of a mixed mode fracture specimen: the asymmetric double cantilever beam. *Journal of Materials Science* **28,** 5620–5629.